

# A Fast Method for Evaluating Green's Function in Irregular Domains with Application to Charge Interaction in a Nanopore

Qiyuan Zhao<sup>1</sup>, Pei Liu<sup>2,3</sup> and Zhenli Xu<sup>2,\*</sup>

<sup>1</sup> Zhiyuan College, Shanghai Jiao Tong University, Shanghai 200240, China.

<sup>2</sup> School of Mathematical Sciences, Institute of Natural Sciences, and MoE Key Lab of Scientific and Engineering Computing, Shanghai Jiao Tong University, Shanghai 200240, China.

<sup>3</sup> Department of Mathematics, Pennsylvania State University, University Park, PA 16802, USA.

Received 29 June 2017; Accepted (in revised version) 30 October 2017

---

**Abstract.** We develop a fast meshless algorithm for electrostatic interaction in an irregular domain with given potential boundary conditions, which is of importance in many applications such as electrochemical energy and electric structure calculations. The algorithm is based on an approximation of the Green's function using two-level image charges, in which the inner-layer charges are located nearby the boundary to eliminate the singularity of the induced polarization potential, and the outer-layer charges with fixed positions approximate the long-range tail of the potential. We find the number of inner-layer image charges can be very small and thus the total complexity of the algorithm is less expensive and potentially suitable for use in particle simulations. The numerical results show the performance of the algorithm is attractive. We also use the algorithm to investigate the electrostatic interaction for particles in a cylindrical nanopore and show that the electrostatic interaction within the pore has an exponential decay.

**AMS subject classifications:** 31B10, 65M80, 78A30

**Key words:** Poisson's equation, image charge methods, meshless algorithm, electrostatic many-body phenomena, Green's function.

---

## 1 Introduction

Electrostatics at interfaces has been the central theme for nanoscale systems such as colloidal suspensions, biomolecules, electrochemical energy devices, and nanoparticle self-assembly [1]. Particle simulations for these systems require a convenient calculation for

---

\*Corresponding author. Email address: xuzl@sjtu.edu.cn (Z. Xu)

the Green's function of Poisson's equation with specified boundary or interface conditions, which gives the electrostatic interaction between particles. The image-charge method (ICM) is unique to provide an analytical representation for given boundary or interface conditions [2]. The ICM has been widely applied in particle simulations for dielectric effects near interfaces [3,4], but it only exists in very limited boundary geometries such as planar interfaces and spheres. The use of the Green's function for irregular boundaries is often avoided in literature, and one solves the Poisson's equation by the grid-based method such as boundary integral method [5–7] in order to do particle simulations with irregular surfaces, which is computationally intensive and is only available for small systems.

In this work, a meshless fast algorithm is proposed for numerical approximation of the Green's function for Poisson's equation in irregular domains with Dirichlet boundary condition. Since the induced potential due to a point source is a harmonic function, we approximate its boundary data by potential functions from fictitious point sources outside the boundary (image charges), and determine the coefficients by requiring the error minimization on the boundary. Historically, this idea with fictitious point sources has been widely discussed as the method of fundamental solutions (MFS) for boundary value problems of differential equations in engineering applications, particularly, for Laplace's equation [8,9], which keeps attracting the latest attention in computational science [10,11]. The new development in the present work is the use of a two-layer ICM approximations for assignment of image-charge locations, and the inner-layer images are determined through an adaptive manner by a nonlinear least squares fitting. Since in the Green's function problem, the induced charge is only singular when the source approaches the boundary, it is found that only a small number of inner-layer images can effectively eliminate the singularity, and thus the nonlinear optimization can be performed rapidly due to the low dimensions. As usual as the MFS, the outer-layer images have fixed locations distributed on a regular surface, and their strengths are determined by solving a linear problem. We show the two-layer algorithm provides very rapid calculations of Green's functions, and thus it is potentially useful for particle simulations of charged systems, which will be the objective of our ongoing work.

The new algorithm is used to investigate the interaction force between ionic particles in nanopores. This problem is of great importance in electrochemical energy devices as the electrode is often made of porous materials and the understanding of ionic interaction within nanopores is essential to enhance the capacitance of the electrode [12]. It is observed that ionic pairwise interaction is exponentially decaying within the nanopore and the decaying rate is comparable to the pore size. This implies that a nanopore is accessible by a large number of likely charged ions and the capacitance is then maximized due to appropriate pore sizes, in agreement with many experimental and simulational suggestions [13–15].

The organization of this paper is as follows. In Section 2, we present the boundary integral expressions for the Green's function with conducting boundary condition on physical boundary and extended boundary, and discuss the numerical algorithm. In

Section 3, numerical examples for different boundary geometries are performed to show the attractive performance of the algorithm, and the algorithm is used to study the charge interaction within a nanopore. Finally, concluding remarks are drawn in Section 4.

## 2 Method

### 2.1 Green's function for Dirichlet boundary condition

Consider the electrostatic potential  $\Phi(\mathbf{r})$  for a system with charge distribution within a vessel domain  $\Omega$  of metallic boundary, which is described by the Poisson's equation,

$$-\nabla^2\Phi(\mathbf{r})=4\pi\rho(\mathbf{r}), \quad \mathbf{r} \in \Omega, \quad (2.1)$$

subject to an electrostatic potential boundary condition  $\Phi(\mathbf{r}) = V(\mathbf{r})$  for  $\mathbf{r} \in \partial\Omega$ , where the charge density is the superposition of  $N$  point charges and a continuous distribution,  $\rho(\mathbf{r}) = \sum_j q_j \delta(\mathbf{r} - \mathbf{r}_j) + \rho_c(\mathbf{r})$  with  $q_j$  being the point charge of the  $j$ th ion at position  $\mathbf{r}_j$ , and  $\rho_c$  can be the electron density or some fixed charge distribution [16]. In electrochemical, biophysical, and soft matter applications [17], the ions are mobile and the Poisson's equation should be solved in each time step for the dynamics of ions, thus a fast Poisson solver is essential for computational research of these systems.

By using the Green's theorem, one can reformulate the Poisson's equation in an integral form [18],

$$\Phi(\mathbf{r}) = \int_{\Omega} \rho(\mathbf{p}) G(\mathbf{r}, \mathbf{p}) d\mathbf{p} - \frac{1}{4\pi} \oint_{\partial\Omega} V(\mathbf{p}) \frac{\partial}{\partial \mathbf{n}_{\mathbf{p}}} G(\mathbf{r}, \mathbf{p}) dS(\mathbf{p}), \quad (2.2)$$

where  $\mathbf{n}_{\mathbf{p}}$  is the unit vector at  $\mathbf{p}$  on the boundary and the Green's function  $G$  is defined by,

$$\begin{cases} -\nabla^2 G(\mathbf{r}, \mathbf{p}) = 4\pi\delta(\mathbf{r} - \mathbf{p}), & \mathbf{r} \in \Omega, \\ G(\mathbf{r}, \mathbf{p}) = 0, & \mathbf{r} \in \partial\Omega. \end{cases} \quad (2.3)$$

It is seen that for the Dirichlet boundary condition the superposition does not hold any more due to the boundary contribution. The electrostatic potential within the domain is determined by Eq. (2.2) if the Green's function can be efficiently solved. The essential step to use the integral formulation is then a fast algorithm for the Green's function (2.3). This integral-equation method is particularly useful for problems in particle simulations [17] as the number of particles may be much smaller than the number of grid points in grid-based methods and the singularities due to that the point sources are close to the boundary are well treated..

The Green's theorem can also be used to write the solution to Eq. (2.3) into an integral form by using the free-space Green's function for the Laplace equation,  $1/|\mathbf{r} - \mathbf{p}|$ ,

$$G(\mathbf{r}, \mathbf{r}') = \frac{1}{|\mathbf{r} - \mathbf{r}'|} + \frac{1}{4\pi} \oint_{\partial\Omega} \frac{\partial G(\mathbf{p}, \mathbf{r}') / \partial \mathbf{n}_{\mathbf{p}}}{|\mathbf{r} - \mathbf{p}|} dS(\mathbf{p}). \quad (2.4)$$

Given the source location  $\mathbf{r}'$ , the surface charge density  $\sigma(\mathbf{p}) = \partial G(\mathbf{p}, \mathbf{r}') / \partial \mathbf{n}_{\mathbf{p}}$  can be determined by numerically solving the boundary integral equation when  $\mathbf{r}$  approaches the boundary. Although boundary integral methods have been widely studied for the Poisson's equation, one will not use it to solve the Green's function  $G$  due to the expensive cost as the calculation should be performed for each  $\mathbf{r}'$  because the boundary integral method is grid-based and it has to use many grid points to resolve the singularity when  $\mathbf{r}'$  approaches the boundary.

In a special case, when the domain is a sphere of radius  $R$ , the Green's function can be exactly represented by using an image charge. Let  $\mathbf{r}' = r' \mathbf{n}'$  and  $\mathbf{r}_K = (R^2/r) \mathbf{n}'$  be the mirror position of the Kelvin transformation, then one has,

$$G(\mathbf{r}, \mathbf{r}') = \frac{1}{|\mathbf{r} - \mathbf{r}'|} + \frac{(-R/r')}{|\mathbf{r} - \mathbf{r}_K|}, \quad (2.5)$$

where the image charge of strength  $-R/r'$  introduces an additional fundamental solution such that the boundary condition in Eq. (2.3) is satisfied.

Physically, the image-charge potential is the induced potential due to the unit source charge at  $\mathbf{r}'$  under the conducting boundary condition [2]. The so-called ICM is a unique method to solve the electrostatic problems, which introduces one or some fictitious charges outside the interested domain to represent the influence due to the boundary condition. It has been studied for different boundary conditions, but limits to regular geometries [19], e.g., dielectric spherical or layered spherical geometries [20–25]. In general, no simple ICM exists for a boundary with irregular shape because the image theory requires the analytical expression of the solution. In the following discussion, we aim to approximate the Green's function by a two-layer ICM. It is a coupling approach of the ICM and the boundary integral method, which shall be efficient for calculating the Green's function as the inner-layer images can resolve the singularity of the point source, and the outer-layer images accurately approximate the long-range tail of the potential.

## 2.2 Boundary integral on an extended domain

Let  $G_{\text{ind}}(\mathbf{r}, \mathbf{r}') = G - 1/|\mathbf{r} - \mathbf{r}'|$  be the induced potential, then  $G_{\text{ind}}$  is a harmonic function in domain  $\Omega$  with boundary value  $G_{\text{ind}} = -1/|\mathbf{r} - \mathbf{r}'|$  for  $\mathbf{r} \in \partial\Omega$ . As shown in Fig. 1, we introduce an artificial boundary such that its enclosed region  $\Omega^e$  satisfies  $\Omega \subset \Omega^e$  and  $\partial\Omega \cap \partial\Omega^e = \emptyset$ . The induced potential can be written by the following integrals,

$$G_{\text{ind}}(\mathbf{r}, \mathbf{r}') = \int_{\Gamma} \frac{q(\mathbf{p})}{|\mathbf{r} - \mathbf{p}|} d\mathbf{p} + \int_{\partial\Omega^e} \frac{\sigma(\mathbf{p})}{|\mathbf{r} - \mathbf{p}|} dS(\mathbf{p}), \quad (2.6)$$

where  $\Gamma$  is a subset inside the complementary set  $\Omega^e \setminus \Omega$ . When  $G_{\text{ind}}$  can be harmonically extended to domain  $\Omega^e$ , then  $\sigma$  is the Dirichlet-to-Neumann mapping [26] of  $G_{\text{ind}}$  on its boundary. Here,  $\Gamma$  is defined as the set where the harmonic extension fails, and  $q$  represents the singularity in the harmonic extension.

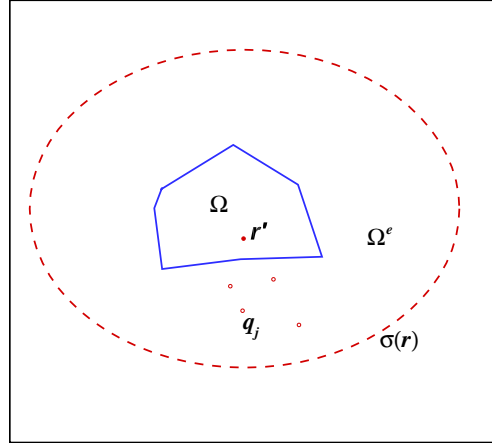


Figure 1: Schematic illustration for the solution of the Green's function. The induced potential due to the source charge at  $\mathbf{r}'$  is approximated by the superposition of point image charges  $q_j$ ,  $j=1, \dots, L$  and surface charge  $\sigma(\mathbf{r})$  on  $\partial\Omega^e$ .

Let  $\hat{\Omega}$  be the domain where the induced potential  $G_{\text{ind}}$  can be harmonically extended within  $\Omega^e$ , then it satisfies  $\Omega \subset \hat{\Omega} \subset \Omega^e$ . If  $\hat{\Omega} = \Omega^e$ , then clearly  $\Gamma = \emptyset$ , and the induced potential can be written as an integral over  $\partial\Omega^e$ . This is very beneficial for numerical approximation since the artificial boundary  $\partial\Omega^e$  is generally of regular shape. If  $\hat{\Omega} \neq \Omega^e$ , then  $G_{\text{ind}}$  can be represented as the integral over  $\partial\hat{\Omega}$ , and thus  $\Gamma$  can take  $\partial\hat{\Omega} \setminus \partial\Omega^e$ . In this case,  $\sigma(\mathbf{r}) = 0$  for  $\mathbf{r} \in \partial\Omega^e \setminus \partial\hat{\Omega}$ .

In general, the singularity of the harmonic extension only happens in a set of zero measure, which will be presented by inner-layer images in this work. Use the spherical domain as an example for which Eq. (2.5) is the exact solution. If  $\mathbf{r}_K$  is not in  $\Omega^e$ , the induced potential  $G_{\text{ind}}(\mathbf{r}, \mathbf{r}') = -(R/r')/|\mathbf{r} - \mathbf{r}_K|$  can be harmonically extended into the whole domain of  $\Omega^e$ , and then  $\Gamma = \emptyset$ . If  $\mathbf{r}_K \in \Omega^e$ , it is also straightforward to see that  $\Gamma = \{\mathbf{r}_K\}$  is simply a set of a single point. Now for the spherical domain, if the boundary conditions are interface conditions across the surface, we can see that the image charges are composed of a point and a line [22]. Similarly, in the case of a cubic box, the image charges are isolated points [27].

To justify the importance of the integral over  $\Gamma$ , let us consider another case:  $\Omega$  and  $\Omega^e$  are two infinite cylinders with radius  $r_1$  and  $r_2$  and their central axes coincide with the  $z$ -axis. In cylindrical coordinates  $(r, \theta, z)$ , suppose that the source point is at  $(r', 0, 0)$  with  $r' < r_1$ . Without taking into account the contribution from  $q(\mathbf{r})$ , Eq. (2.6) becomes,

$$\int_{\partial\Omega^e} \sigma(\theta_1, z_1) g(\theta_1 - \theta_2, z_1 - z_2) d\theta_2 dz_2 = f(\theta_1, z_1), \quad (2.7)$$

for every  $(\theta_1, z_1)$  on  $\partial\Omega_1$ , where,

$$g(\theta, z) = \frac{1}{\sqrt{r_1^2 + r_2^2 - 2r_1 r_2 \cos\theta + z^2}} \quad (2.8)$$

and,

$$f(\theta, z) = -\frac{1}{\sqrt{r_1^2 + r'^2 - 2r_1 r' \cos \theta + z^2}} \quad (2.9)$$

are the expressions for the free-space Green's function and the induced potential on the surface, respectively.

In order to study the solution of  $\sigma$ , one could use the Fourier series expansion. Let  $\hat{g}_\theta(j, z)$  and  $\hat{g}_z(\theta, k)$  be the Fourier coefficients of  $g$  for  $\theta$  and  $z$  coordinates, respectively. Then, by some calculations their leading asymptotics for the high-frequency limit are expressed as,

$$\begin{cases} \hat{g}_\theta(j, z) \sim \frac{\pi}{2} \sqrt{\frac{2}{r_1 r_2 j}} \left( \frac{r_1^2 + r_2^2 + z^2}{2r_1 r_2} + \sqrt{\left( \frac{r_1^2 + r_2^2 + z^2}{2r_1 r_2} \right)^2 - 1} \right)^{-j}, & \text{as } j \rightarrow \infty, \\ \hat{g}_z(\theta, k) \sim \frac{\pi/2}{(r_1^2 + r_2^2 - 2r_1 r_2 \cos \theta)^{1/4}} \sqrt{\frac{2}{k}} e^{-k(r_1^2 + r_2^2 - 2r_1 r_2 \cos \theta)^{1/2}}, & \text{as } k \rightarrow \infty. \end{cases} \quad (2.10)$$

Similarly, for  $f$ , we have,

$$\begin{cases} \hat{f}_\theta(j, z) \sim -\frac{\pi}{2} \sqrt{\frac{2}{r_1 r' j}} \left( \frac{r_1^2 + r'^2 + z^2}{2r_1 r'} + \sqrt{\left( \frac{r_1^2 + r'^2 + z^2}{2r_1 r'} \right)^2 - 1} \right)^{-j}, & \text{as } j \rightarrow \infty, \\ \hat{f}_z(\theta, k) \sim -\frac{\pi/2}{(r_1^2 + r'^2 - 2r_1 r' \cos \theta)^{1/4}} \sqrt{\frac{2}{k}} e^{-k(r_1^2 + r'^2 - 2r_1 r' \cos \theta)^{1/2}}, & \text{as } k \rightarrow \infty. \end{cases} \quad (2.11)$$

From these asymptotics, it is clear that when  $r_3 < r_1^2/r_2$ , the Fourier coefficients of  $\sigma(\theta, z)$ , i.e.,  $\hat{\sigma}_\theta = \hat{f}_\theta/\hat{g}_\theta$  and  $\hat{\sigma}_z = \hat{f}_z/\hat{g}_z$ , tend to zero as  $j$  and  $k \rightarrow \infty$ , and the solution of the integral equation (2.7) exists. From Eq. (2.11) it is not difficult to observe that the truncation error for the Fourier expansion of  $\sigma$  at  $j = k = \sqrt{N}$  is in the order of  $N^{-1/4} (r'/r_1)^N$ , which converges very fast when  $r'$  is smaller than  $r_1$ . When  $r_3 \geq r_1^2/r_2$ , however, the Fourier coefficients of  $\sigma(\theta, z)$  do not tend to zero as  $j \rightarrow \infty$ . Therefore, the solution of the integral equation (2.7) does not exist. In this case, the singularity between  $\partial\Omega$  and  $\partial\Omega^e$  must be taken into account. It is then necessary to find a proper approximation for the integral on  $\Gamma$  in order to correctly solve the induced potential.

### 2.3 A two-layer image-charge method

The induced potential  $G_{\text{ind}}$  is approximated by a two-layer ICM based on the boundary integral expression with the extended domain, Eq. (2.6), as is shown in Fig. 1. Let  $\{(q_\ell, \mathbf{r}_\ell)\}_{\ell=1}^L$  be the strengths and positions of  $L$  image charges that approximate the integral over  $\Gamma$ . These image charges are called inner-layer images. Let  $\Omega^e$  be a domain of regular geometry with  $N$  collocation points  $\{\mathbf{R}_i\}_{i=1}^N$  on its boundary. Suppose the collocation points on  $\partial\Omega^e$  are given, the charges  $\{Q_i\}_{i=1}^N$  are to be determined, and we call these

points the outer-layer images. In this work, the collocation points are obtained by simulated annealing [28] of repulsive particles up to low temperature such that these points are almost uniformly distributed on  $\partial\Omega^e$ . The approximate induced potential within domain  $\Omega$  is then given by,

$$\tilde{G}_{\text{ind}} = \sum_{\ell=1}^L \frac{q_{\ell}}{|\mathbf{r} - \mathbf{r}_{\ell}|} + \sum_{i=1}^N \frac{Q_i}{|\mathbf{r} - \mathbf{R}_i|}, \quad (2.12)$$

where  $\{q_{\ell}, \mathbf{r}_{\ell}, \ell=1, \dots, L; Q_i, i=1, \dots, N\}$  are to be calculated numerically.

Different from the idea of the multilayer method [10] for the Laplace equation where multiple fictitious boundaries are introduced to obtain accurate solutions, we determine adaptively the inner-layer images near the source since in this region the induced potential can be singular. We expect that a small number of inner-layer images can achieve this goal, i.e.,  $L \ll N$ . In principle, one shall use the boundary data of the induced potential,  $G_{\text{ind}} = -1/|\mathbf{r} - \mathbf{r}'|$  for  $\mathbf{r} \in \partial\Omega$ , and these parameters of the charge locations and strengths of all images are determined by minimizing the  $L_2$  error over the boundary,  $E = \|\tilde{G}_{\text{ind}} - G_{\text{ind}}\|_2$  on  $\partial\Omega$ . This leads to a nonlinear problem of high dimensions, and thus the computational cost is intensive. For the purpose of rapid calculation, we solve for the parameters of the inner-layer and outer-layer images separately, and develop a new two-step algorithm to approximate the solution.

Let  $\{\mathbf{x}_j\}_{j=1}^M$  be  $M$  monitoring points on boundary  $\partial\Omega$ . At the first step of the algorithm, we suppose that the superposition of the inner-layer images provides an estimate of the induced potential and the parameters of these images are solved by minimizing the total error of the monitoring points. Let

$$\phi(\mathbf{r}) = \sum_{\ell=1}^L \frac{q_{\ell}}{|\mathbf{r} - \mathbf{r}_{\ell}|} + \frac{1}{|\mathbf{r} - \mathbf{r}'|} \quad (2.13)$$

be the potential distribution from the sum of the source and the inner-layer image charges. Then the parameters are solved by,

$$\{(q_{\ell}, \mathbf{r}_{\ell})\}_{\ell=1}^L = \operatorname{argmin} \sum_{j=1}^M [\phi(\mathbf{x}_j)]^2. \quad (2.14)$$

The image points are searched in domain  $\Omega^e \setminus \Omega$ . Since the gradient of the objective function can be exactly determined in a simple way, the steepest descent method is employed to calculate a locally optimal solution. In practice, the initial guess of the parameters depends on the geometry of the boundary and the locations are usually set near the source point. Since the accuracy of the algorithm is not sensitive to this step, the iteration is terminated when the objective function is less than a threshold value  $10^{-6}$ , and in addition one can use smaller number of monitoring points in the objective function (2.14) to reduce the computational cost.

Secondly, we solve for the outer-layer images. As the locations  $\{\mathbf{R}_i\}_{i=1}^N$  are pre-specified, this step calculates the strengths of these charges by solving a linear system



of equations, which aims to minimize the total error of these charges on the boundary  $\partial\Omega$ . Let  $\mathbf{A}$  be the  $M \times N$  matrix with identity  $A_{ji} = 1/|\mathbf{x}_j - \mathbf{R}_i|$ , the charge vector  $\mathbf{y} = (Q_1, \dots, Q_N)^T$ , and vector  $\mathbf{b} = (\phi(\mathbf{x}_1), \dots, \phi(\mathbf{x}_M))^T$  be the potential due to the source and the inner-layer images. The method of least squares is used to minimize the  $L_2$  norm of the total contribution from monitoring points on the boundary,  $(\mathbf{A}\mathbf{y} + \mathbf{b})$ . Since the condition number of the coefficient matrix can be big, the SVD decomposition is employed to solve the least squares problem; see Lin *et al.* [11] and reference therein for discussion on fast MSF numerical algebra method.

The nonlinear optimization method for image charges has been used in literature. In a recent work [29], the ICM method was developed by fitting the harmonic expansion for the cylindrical geometry with dielectric jump conditions on the surface. Since only the step for inner-layer images is employed, it was reported that this leads to an error of around 1% in the self energy calculation. In Example 3 of next section, it is shown that the two-level ICM can greatly improve the accuracy in comparison to this method.

### 3 Numerical results

We show the performance of the algorithm by using three numerical examples with domain  $\Omega$  as sphere, cube and cylindrical objects, respectively. We compute the errors for different locations of the source. In all calculations, the monitoring points  $\{\mathbf{x}_j\}_{j=1}^M$  on  $\partial\Omega$  and collocation points  $\{\mathbf{R}_i\}_{i=1}^N$  on  $\partial\Omega^e$  are obtained by running Monte Carlo simulated annealing [28] for repulsive particles on the surface. The zero-temperature limit of simulations leads to a quasi-crystal structure of particles which are considered as the monitoring and collocation points. In the step of determining inner-layer images, only partial monitoring points are included in the objective function, and those points close to the source points are used. Let  $D = \min\{|\mathbf{x}_j - \mathbf{r}'|, j=1, \dots, M\}$  be the minimum distance. We choose those points satisfying  $|\mathbf{x}_j - \mathbf{r}'| < 3D$  as the monitoring points in the calculations. All three examples use the Dirichlet boundary condition except that in the case of spherical geometry we also extend the method for the case of the Robin boundary condition.

**Example 1 (Spherical geometry).** We consider the case of  $\Omega$  being a sphere of radius  $R = 1$  and a source charge located at  $(0, 0, r')$  within the sphere. The induced potential is calculated by the two-layer ICM, where the number of the inner-layer image is  $L = 1$ . The extended domain  $\Omega^e$  is also a concentric sphere of radius 2. We calculate the induced potential for two cases,  $r' = 0.7$  and  $0.9$ , where the absolute error function,  $\mathcal{E}(\mathbf{r}) = |\tilde{G}_{\text{ind}} - G_{\text{ind}}|$ , is used to measure the accuracy performance. For comparison, we calculate the results without putting an inner-layer image  $L = 0$ . Fig. 2 illustrates the error distribution over a cross section for the four cases with two different  $r'$  and  $L$  and  $N = 1600$  is fixed. It can be seen that when  $r'$  approaches the boundary, the inner-layer image is required as the induced potential is the potential due to a charge at  $1/r'$ , which is singular in domain



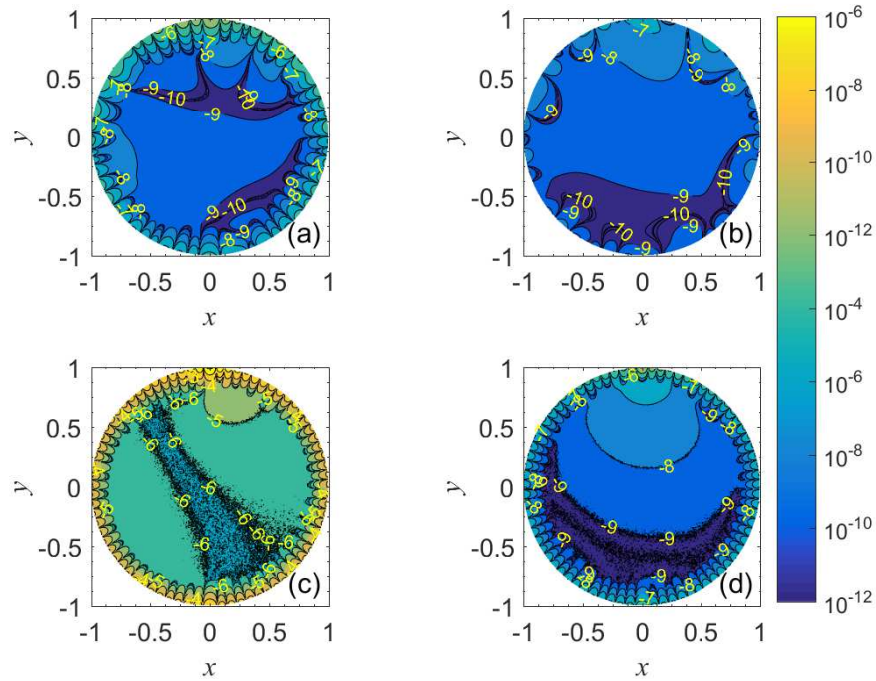


Figure 2: Error distribution of the induced potential in a cross section at  $(x,y,0)$  plane within the unit sphere for a source charge located at  $(0,0,r')$ , respectively. (a)  $r'=0.7$  without inner-layer image; (b)  $r'=0.7$  with one inner-layer image; (c)  $r'=0.9$  without inner-layer image; (d)  $r'=0.9$  with one inner-layer image. The numbers on contours represent the logarithm of the error value.

$\Omega^e$ . Even when  $r'$  is small such that the Kelvin image point is outside  $\Omega^e$ , the inner-layer image is still useful to improve the accuracy when the number of outer-layer images is the same by comparing panels (c) and (d).

As is known, the exact solution can be represented by an image charge located at the Kelvin image point. When  $r' < 0.5$ , the image charge is located outside  $\partial\Omega^e$  and the induced potential can be exactly represented by a surface charge on  $\partial\Omega^e$ . In order to investigate the influence of the inner-layer image, we show the maximum error as function of the outer-layer image number  $N$  for four different  $r'$  from 0.1 to 0.8 in Fig. 3(ab). It is observed that when  $r' < 0.5$ , the accuracy for  $L=0$  case can be very high as long as  $N$  is large enough (the error rapidly drops to  $10^{-6}$  when  $N > 200$ ). It is also seen that in this case an additional image can further improve the accuracy. In contrast, if  $r' > 0.5$ , the convergence for  $L=0$  case is slow and the inclusion of the inner-layer image is crucial for the approximation of the induced potential.

In order to investigate the sensitivity of the solution on the location of the inner-layer

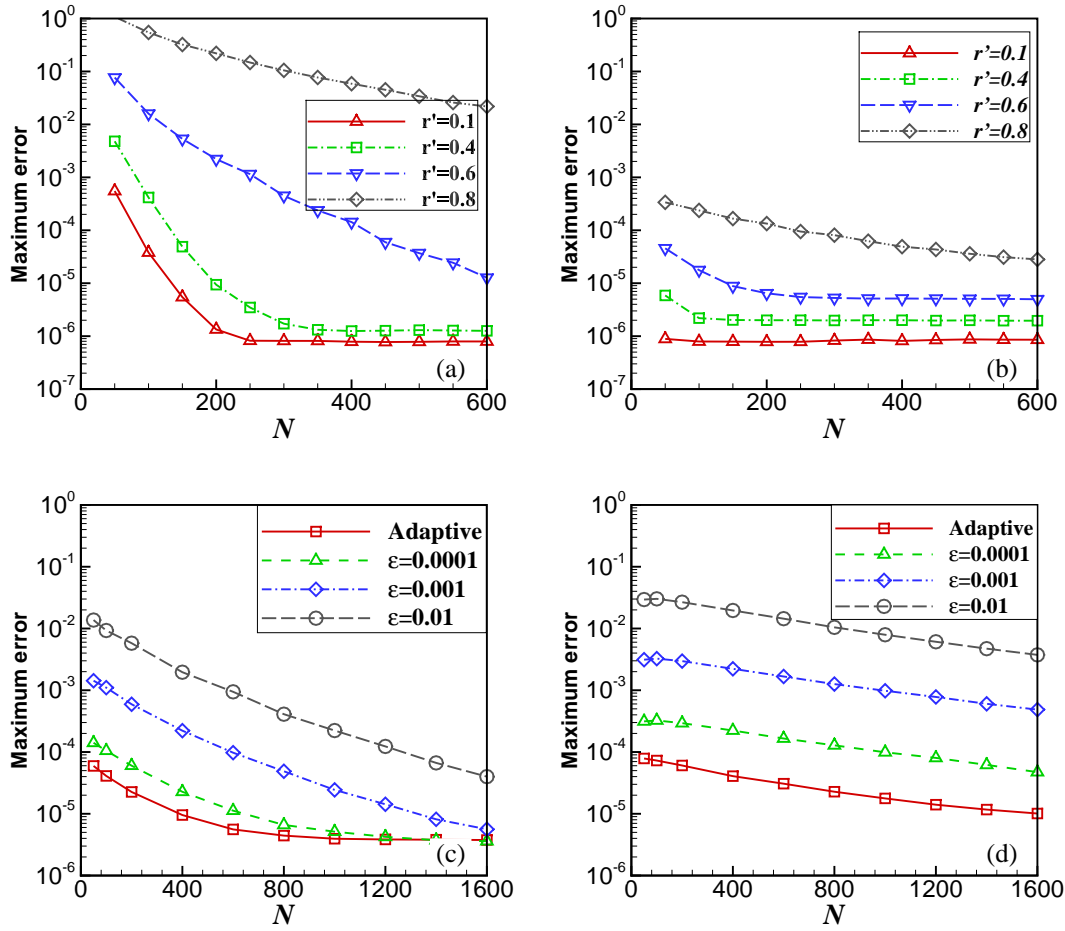


Figure 3: (ab) Maximum errors for different source locations as functions of number of outer-layer images for  $L=0$  (a) and  $L=1$  (b); (cd) Maximum errors for different perturbations for the inner-layer image and those adaptively determined using optimization searching for the source charge located at  $r'=0.8$  (c) and  $0.9$  (d).

image. We consider to fix the inner-layer image and its strength as

$$\mathbf{r}_1 = \left( 0, 0, (1+\epsilon) \frac{R^2}{r'} \right), \quad \text{and} \quad q_1 = -\frac{R^2(1+\epsilon) - Rr'}{r'(R-r')} \quad (3.1)$$

for a small  $\epsilon$ , i.e., a slight variation of the Kelvin image point. This setting remains the boundary value at  $(0,0,1)$  since the sum of the source and the image potential at this point is zero. The solution is then calculated by increasing the number of the outer-layer images to improve the accuracy. The different source locations  $r'=0.8$  and  $0.9$  are studied. Fig. 3(cd) shows the error results for three different  $\epsilon$ , together with the developed algorithm which adaptively determines the inner-layer image. The comparison demonstrates

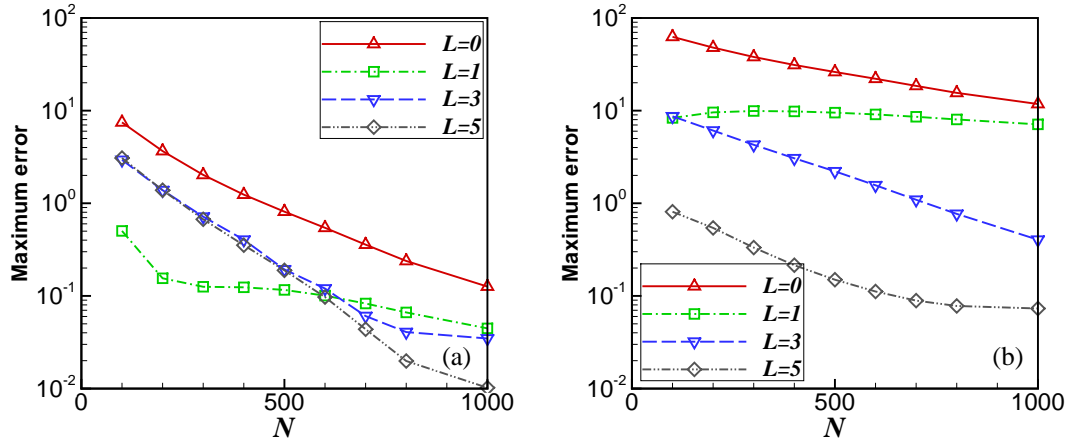


Figure 4: Maximum errors for different number of the inner-layer images with the increase of the outer-layer images for the case of the Robin boundary condition. The source charge is located at (a)  $r' = 0.8$  and (b)  $r' = 0.9$ , respectively.

the optimization method can accurately determine the location of the image charge and thus provides high-precision approximation of the reduced potential.

This paper focuses the discussion on the Dirichlet boundary condition. The two-layer ICM can be straightforwardly extended to other boundary conditions. To show it, we give an example of the Robin boundary condition using the same setup as above but the boundary condition for the Green's function,  $\nabla G \cdot \mathbf{n} + G = 0$ , on the spherical surface. The only difference is the objective function in Eq. (2.14), which becomes  $\sum_{j=1}^M [\nabla \phi(\mathbf{x}_j) \cdot \mathbf{n}(\mathbf{x}_j) + \phi(\mathbf{x}_j)]$  with the potential function  $\phi$  defined by Eq. (2.13). We calculate the solutions with the two-layer ICM, and compared them with the exact solution,

$$G_{\text{ind}}(\mathbf{r}, \mathbf{r}') = \sum_{n=0}^{\infty} \frac{n+1-R}{n+R} \frac{(rr')^n}{R^{2n+1}} P_n(\cos \theta), \quad (3.2)$$

where  $\theta$  is the angle between  $\mathbf{r}$  and  $\mathbf{r}'$ ,  $P_n(\cdot)$  are the Legendre polynomials, and we take  $R=1$  and truncate the series at  $n=100$ . The induced potential can be actually represented by an image point charge at  $\mathbf{r}_K$  and an image line charge from  $\mathbf{r}_K$  to infinity by following the procedure in Cai *et al.* [22]. Fig. 4 illustrates the maximum errors with two different source locations  $r' = 0.8$  and  $0.9$ . In each panel, the solutions are calculated for  $L=0 \sim 5$ , and  $N$  increases from 100 to 1000. The results show a significant increase in accuracy with the increase  $L$  and  $N$ , and demonstrate that the two-layer ICM works well for the Robin boundary condition.

**Example 2 (Cubic box).** In this example, domain  $\Omega$  is a cubic box of size  $[-1, 1]^3$  and the source charge is at the diagonal line  $(1, 1, 1)d$  with  $0 < d < 1$ . In the calculation using the two-layer ICM, we take domain  $\Omega^e$  being a sphere of radius 3 centered at the origin. The

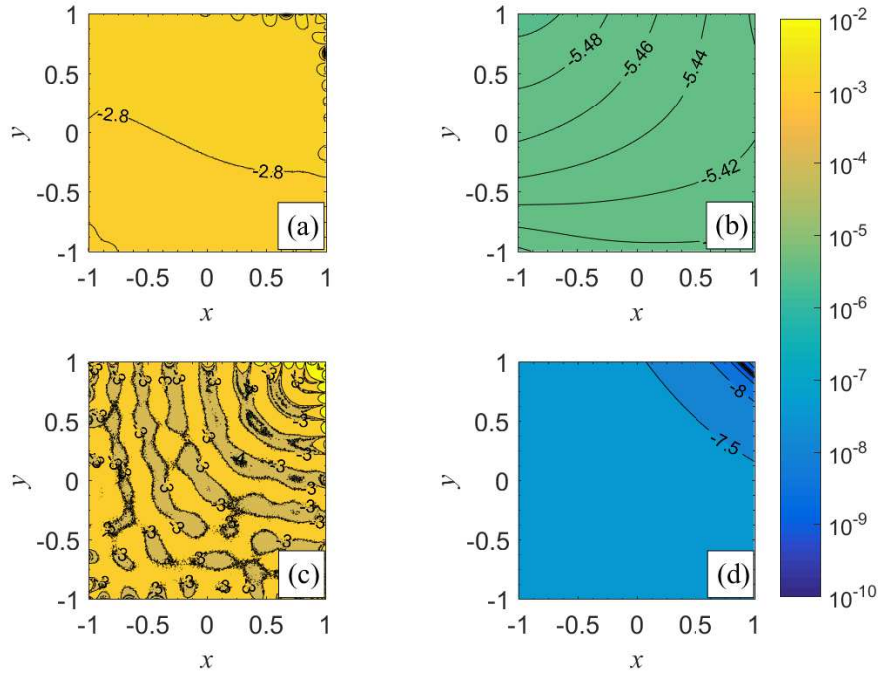


Figure 5: Absolute error of the induced potential in cubic box for a source charge at  $\mathbf{r}' = (1,1,1)d$ . The error in the cross section  $z=d$  is shown. (a)  $d=0.7$  without inner-layer images; (b)  $d=0.7$  with inner-layer images; (c)  $d=0.9$  without inner-layer images; (d)  $d=0.9$  with inner-layer images. The numbers on contours represent the logarithm of the error value.

exact solution of this problem can be found using infinite image charges by the iterative reflection of planar images from different boundaries [27]. We use 7 images within the spherical boundary  $\partial\Omega^e$  as the inner-layer images. These images are those close to the corner  $(1,1,1)$ . In the calculations, these images have fixed positions and charges in order to study the convergence with the number of the outer-layer images. For comparison, the case without the inner-layer images ( $L=0$ ) is computed.

In Fig. 5, the results without and with the inner-layer images are plotted for two different source locations  $d=0.7$  and  $0.9$ . They are shown as the error distribution for the induced potential over a cross section  $z=d$ . Similar to the case of the spherical geometry, the results show that the use of the inner-layer images is essential in improving the accuracy of approximation, in particular, when the source charge is close to the boundary.

Fig. 6(ab) displays the error in self-energy of the unit source charge as function of  $d$  for five different outer-layer image numbers  $N=100\sim 1600$ . For comparison, we also calculate the Poisson's equation by the grid-based finite-difference method (FDM) [30] with grid sizes  $\Delta x = \Delta y = \Delta z = 0.05$ . In the finite-difference discretization, the delta function is distributed into the eight nearby grids such that the total amount of charge remains

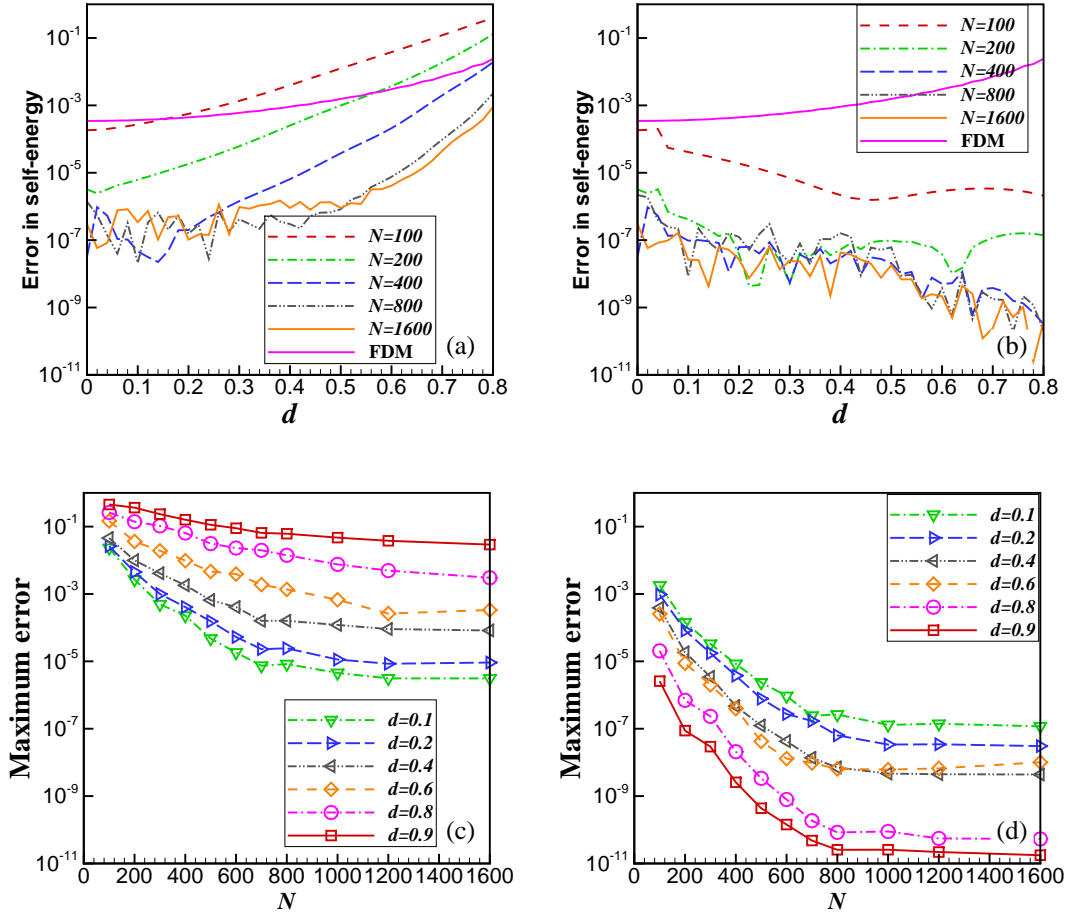


Figure 6: (ab) Absolute error of the self-energy for the source charge located at  $(1,1,1)d$  as function of  $d$ : (a) without inner-layer images, and (b) with 7 inner-layer images. (cd) Maximum error in the induced potential for the source charge located at  $(1,1,1)d$  with 6 different  $d$  as function of  $N$ : (c) without inner-layer images, and (d) with 7 inner-layer images.

one. It is observed that in the  $L=0$  case the error in self-energy increases when  $\mathbf{r}'$  is away from the center. By comparing the results with those of the FDM, it clearly shows that the ICM provides much higher accuracy due to the difficulty of the solution singularity in the finite-difference approximation. It is interesting to observe that the ICM is actually more accurate if the source point is closer to the boundary or corner of the cubic box. In Fig. 6(cd), we plot the convergence with the outer-layer image number,  $N$ , for different source locations.

**Example 3 (Cylindrical geometry).** In this example, domain  $\Omega = \{(x,y,z) : x^2 + y^2 \leq 1 \text{ and } |z| \leq H/2\}$  is a finite cylindrical geometry of radius  $R=1$  and height  $H$ . The source

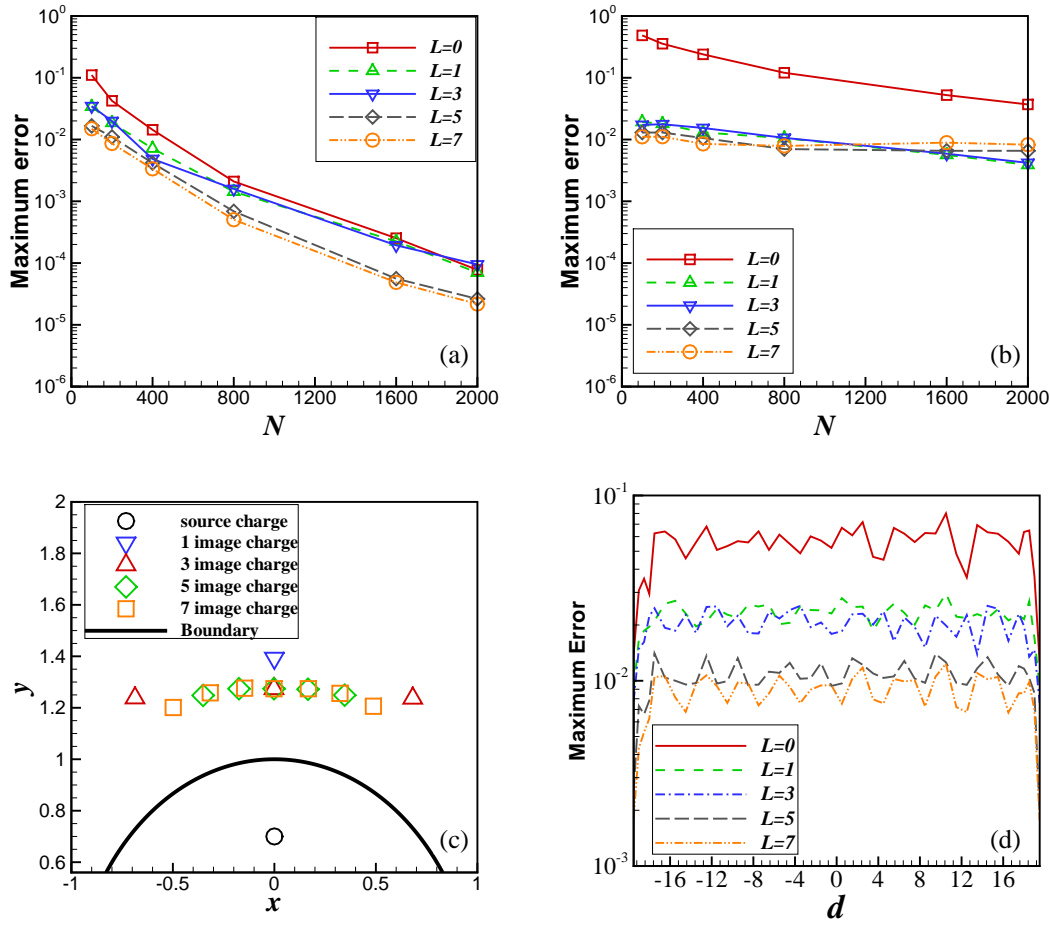


Figure 7: (a) Relative error of induced potential for the case of  $r' = 0.7$ ; (b) Relative maximum error for the case of  $r' = 0.9$ ; (c) Locations of inner-layer images for the case of  $r' = 0.7$ ; (d) Relative maximum error for a long cylinder of height  $H = 40$  for source charge at  $(0, 0.7, d)$  as function of  $d$ .

charge is at  $\mathbf{r}' = (0, r', d)$ . We first consider the case of  $H = 2$  and  $d = 0$ . This is a more difficult problem as the symmetry is broken due to the finite cylinder. We compute the solution for  $L = 0 \sim 7$  and varying  $N$  with two cases of the source locations  $r' = 0.7$  and  $0.9$ . In the calculations, the fictitious domain takes a sphere of radius 2 centered at the origin, and the initial positions of images are placed at an arc of radius  $1 + r'$  on the cross section of  $z = 0$ . Fig. 7(ab) shows the relative maximum error of the induced potential on the cylindrical boundary,  $\max |\hat{G}_{\text{ind}} - G_{\text{ind}}| / \max |\hat{G}_{\text{ind}}|$ , for different number of inner-layer images as function of  $N$ . The results for  $r' = 0.7$  demonstrate the convergence with the increase of  $L$  and  $N$ . Fig. 7(c) displays the locations of the inner-layer images as they are also on the same plane of  $z = 0$ . For  $r' = 0.9$  shown in Fig. 7(b), there is a significant

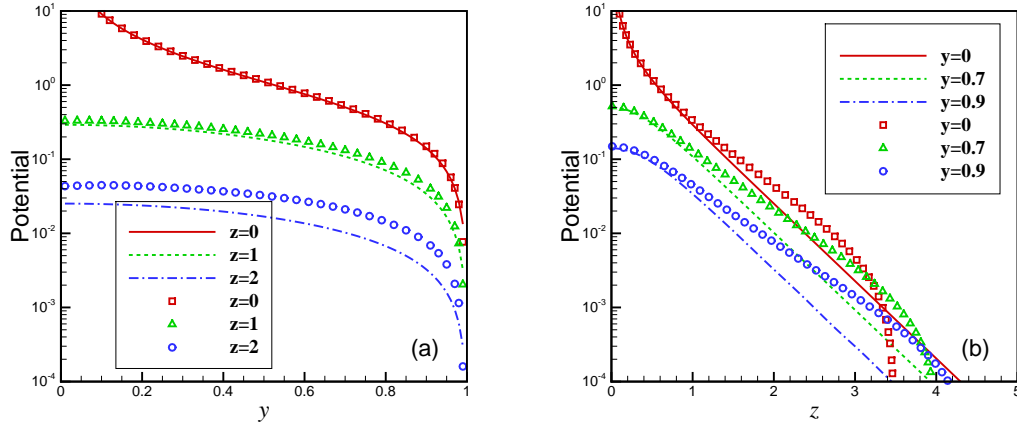


Figure 8: Electrostatic potential due to a source at the center of the long center. (a)  $\phi(0,y,z)$  as a function of  $y$  for  $z=0,1$  and  $2$ ; (b)  $\phi(0,y,z)$  as a function of  $z$  for  $y=0,0.7$  and  $0.9$ . The lines represents the two-layer ICM, and the symbols represent the method with only inner-layer images.

increase in accuracy with the use of the inner-layer images, i.e.,  $L > 0$ . The maximum error remains around 1%, showing a slow convergence of the error with the increase of  $L$  and  $N$ . The reason for the slow convergence is possibly due to the local optimization used in searching the inner-layer images, and to improve it we should use a method which can find the global minimization solution. We also compute the solution for a long cylinder of  $H=40$ , for which the relative maximum errors are illustrated in Fig. 7(d) as function of  $d$ . In the calculations, an ellipsoid with three axis lengths 2, 2 and 40, and the number of outer-layer images is fixed with  $n=3200$ . It is seen that the maximum error is decreased with the increase of  $L$ .

Finally, as an application we investigate the pairwise interaction between charges in a confined geometry, which is of great importance in ion channels and nano-materials applications [1, 31]. It has been shown that the polarization effect could lead to the counterintuitive attraction between likely charged particles when there exists asymmetry in particle valence or sizes [32–34]. Under a confinement such as a cylindrical pore, the electrostatic interaction behaves quite differently from the direct Coulomb interaction, since the Dirichlet boundary condition provides an attraction to the charge and screens the interaction between charges. We consider the same cylindrical geometry as above with radius  $R=1$  and height  $H=40$ . A source point of unit charge is placed at the center of the long cylinder. We use a large extended domain which is an ellipsoid of axis lengths 5, 5 and 100, and set 8634 monitoring points quasi-uniformly on the surface of the cylinder and 3200 outer-layer images on the ellipsoidal surface. Since the charge is at the center, no inner-layer image is used, and the algorithm can still provide an accuracy of the maximum error  $\sim 10^{-4}$  by additional test. Fig. 8 (lines) displays the electrostatic potential due to the charge. Both panels illustrate the short-range potential, different from the  $1/r$



long-range potential in free space. It is intuitive to see the rapid decaying along the  $y$  direction due to the image charge repulsion, as shown in Fig. 8(a). Along the  $z$  direction, it is clearly shown that the electrostatic potential  $G(\mathbf{r}, \mathbf{r}')$  decays exponentially and the decay rate is at the order of cylindrical radius. This exponential decay phenomenon can be very useful in applications. For example in electrochemical energy devices [12, 13], this property implies that many like-charged particles can be put in a porous electrode and thus the capacitance of the electrode can be greatly enhanced. For comparison, the ICM with only inner-layer images [29] which approximate the cylindrical harmonics series [35] are present as symbols in Fig. 8 where six image charges are used for each source. Clearly, the method in Ref. [29] cannot produce the exponential screening for the interaction of large separation, which is much less accurate than the two-layer ICM developed in this paper.

## 4 Conclusions

We have developed a two-layer ICM for the rapid evaluation of the Green's function in electrostatic interaction with given potential boundary conditions. Since the algorithm is shown promising by numerical examples, it is potentially useful for particle simulations of charged systems, e.g., the simulations of electrochemical energy devices, which will be the central issue of the future work. The algorithm is used to study the ionic interaction within a nanopore, demonstrating the exponential decaying of the potential when the ion separation is comparable to the size of the cylindrical pore. This finding explains the capacitance enhancement of using the porous materials as the electrode of supercapacitors. The paper presents very preliminary research of the algorithm. There is much space to improve the algorithm in the future study, e.g., the acceleration algorithm for the nonlinear optimization and the matrix computation for the least squares. This paper focuses on the metallic boundary condition. We also present an example to show the algorithm works for the Robin boundary, and certainly the two-layer ICM can be extended to problems with dielectric boundary.

## Acknowledgments

The authors acknowledge the financial support from the Natural Science Foundation of China (Grant Nos: 11571236 and 21773165) and the support from the HPC center of Shanghai Jiao Tong University. The authors acknowledge the referees for valuable suggestions which improve the paper.

## References

- [1] R. H. French, V. A. Parsegian, R. Podgornik, R. F. Rajter, A. Jagota, J. Luo, D. Asthagiri, M. K. Chaudhury, Y.-M. Chiang, S. Granick, S. Kalinin, M. Kardar, R. Kjellander, D. C. Langreth,

- J. Lewis, S. Lustig, D. Wesolowski, J. S. Wettlaufer, W.-Y. Ching, M. Finnis, F. Houlihan, O. A. von Lilienfeld, C. J. van Oss, T. Zemb, Long range interactions in nanoscale science, *Rev. Mod. Phys.* 82 (2) (2010) 1887–1944.
- [2] J. D. Jackson, *Classical Electrodynamics* (3rd Edition), John Wiley & Sons, New York, 2001.
- [3] R. Messina, Electrostatics in soft matter, *J. Phys. Condens. Matter* 21 (2009) 113102.
- [4] Z. Gan, H. Wu, K. Barros, Z. Xu, E. Luijten, Comparison of efficient techniques for the simulation of dielectric objects in electrolytes, *J. Comput. Phys.* 291 (2015) 317 – 333.
- [5] D. Boda, D. Gillespie, W. Nonner, D. Henderson, B. Eisenberg, Computing induced charges in inhomogeneous dielectric media: Application in a Monte Carlo simulation of complex ionic systems, *Phys. Rev. E* 69 (2004) 046702.
- [6] S. Tyagi, M. Sützen, M. Sega, M. Barbosa, S. S. Kantorovich, C. Holm, An iterative, fast, linear-scaling method for computing induced charges on arbitrary dielectric boundaries, *J. Chem. Phys.* 132 (2010) 154112.
- [7] K. Barros, E. Luijten, Dielectric effects in the self-assembly of binary colloidal aggregates, *Phys. Rev. Lett.* 113 (1) (2014) 017801.
- [8] V. D. Kupradze, M. A. Aleksidze, The method of functional equations for the approximate solution of certain boundary value problems, *USSR Comput. Math. Math. Phys.* 4 (1964) 82–126.
- [9] G. Fairweather, A. Karageorghis, The method of fundamental solutions for elliptic boundary value problems, *Adv. Comput. Math.* 9 (1998) 69–95.
- [10] T. Shigeta, D. L. Young, C.-S. Liu, Adaptive multilayer method of fundamental solutions using a weighted greedy QR decomposition for the Laplace equation, *J. Comput. Phys.* 231 (2012) 7118–7132.
- [11] J. Lin, C. S. Chen, C.-S. Liu, Fast solution of three-dimensional modified Helmholtz equations by the method of fundamental solutions, *Commun. Comput. Phys.* 20 (2016) 512–533.
- [12] J. Huang, B. G. Sumpter, V. Meunier, Theoretical model for nanoporous carbon supercapacitors, *Angew. Chem. Int. Ed.* 47 (3) (2008) 520–524. doi:10.1002/anie.200703864.
- [13] J. Chmiola, G. Yushin, Y. Gogotsi, C. Portet, P. Simon, P.-L. Taberna, Anomalous increase in carbon capacitance at pore size below 1 nm, *Science* 313 (2006) 1760–1763.
- [14] S. Kondrat, N. Georgi, M. V. Fedorov, A. A. Kornyshev, A superionic state in nano-porous double-layer capacitors: insights from monte carlo simulations, *Phys. Chem. Chem. Phys.* 13 (2011) 11359–11366.
- [15] C. Largeot, C. Portet, J. Chmiola, P. L. Taberna, Y. Gogotsi, P. Simon, Relation between the ion size and pore size for an electric double-layer capacitor, *J. Am. Chem. Soc.* 130 (2008) 2730–2731.
- [16] M. Lee, K. Leiter, C. Eisner, J. Knap, Atom-partitioned multipole expansions for electrostatic potential boundary conditions, *J. Comput. Phys.* 328 (2017) 344–353.
- [17] D. Frenkel, B. Smit, *Understanding molecular simulation: From algorithms to applications*, Academic Press, New York, 2002.
- [18] W. Cai, *Computational Methods for Electromagnetic Phenomena: Electrostatics in Solvations, Scattering, and Electron Transport*, Cambridge University Press, Cambridge, 2013.
- [19] Z. Xu, W. Cai, Fast analytical methods for macroscopic electrostatic models in biomolecular simulations, *SIAM Rev.* 53 (2011) 683–720.
- [20] C. Neumann, *Hydrodynamische untersuchungen: Nebst einem anhang über die probleme der elektrostik und der magnetischen induction*, Teubner, Leipzig (1883) 279–282.
- [21] I. V. Lindell, Electrostatic image theory for the dielectric sphere, *Radio Sci.* 27 (1992) 1–8.
- [22] W. Cai, S. Deng, D. Jacobs, Extending the fast multipole method to charges inside or outside

- a dielectric sphere, *J. Comput. Phys.* 223 (2007) 846–864.
- [23] M. Ma, Z. Gan, Z. Xu, Ion structure near a core-shell dielectric nanoparticle, *Phys. Rev. Lett.* 118 (2017) 076102.
  - [24] I. V. Lindell, M. E. Ermutlu, A. H. Sihvola, Electrostatic image theory for layered dielectric sphere, *Microwaves, Antennas and Propagation, IEE Proc.-H* 139 (1992) 186–192.
  - [25] J. Qin, J. J. de Pablo, K. F. Freed, Image method for induced surface charge from many-body system of dielectric spheres, *J. Chem. Phys.* 145 (2016) 124903.
  - [26] H. Han, X. Wu, *Artificial Boundary Method*, Tsinghua University Press, Beijing, 2013.
  - [27] P. K. Yang, S. H. Liaw, C. Lim, Representing an infinite solvent system with a rectangular finite system using image charges, *J. Phys. Chem. B* 106 (2002) 2973–2982.
  - [28] J. S. Liu, *Monte Carlo Strategies in Scientific Computing*, Springer-Verlag, New York, 2001.
  - [29] Z. Xu, W. Cai, X. Cheng, Image charge method for reaction fields in a hybrid ion-channel model, *Commun. Comput. Phys.* 9 (2011) 1056–1070.
  - [30] W. Im, D. Beglov, B. Roux, Continuum solvation model: Computation of electrostatic forces from numerical solutions to the Poisson-Boltzmann equation, *Comput. Phys. Commun.* 111 (1998) 59–75.
  - [31] D. A. Walker, B. Kowalczyk, M. O. de la Cruz, B. A. Grzybowski, Electrostatics at the nanoscale, *Nanoscale* 3 (2011) 1316–1344.
  - [32] E. Bichoutskaia, A. L. Boatwright, A. Khachatourian, A. J. Stace, Electrostatic analysis of the interactions between charged particles of dielectric materials, *J. Chem. Phys.* 133 (2010) 024105.
  - [33] J. Lekner, Electrostatics of two charged conducting spheres, *Proc. Royal Soc. A* 468 (2012) 2829–2848.
  - [34] Z. Xu, Electrostatic interaction in the presence of dielectric interfaces and polarization-induced like-charge attraction, *Phys. Rev. E* 87 (2013) 013307.
  - [35] S. T. Cui, Electrostatic potential in cylindrical dielectric media using the image charge method, *Mol. Phys.* 104 (2006) 2993–3001.